

# Mathematical properties and physical meaning of the gravity gradient tensor eigenvalues

**Carlos Cevallos\***

Consultant

PO Box 955, West Perth WA 6872, Australia

cevallos54@hotmail.com

## SUMMARY

The eigenvalues of the gravity gradient tensor can be expressed as functions of two parameters: a magnitude and a phase. The decomposition gives physical meaning to the eigenvalues: the magnitude measures the amount of curvature and the phase is related to the type of source. Their understanding allows to propose new quantities to interpret. As an example, a modified phase eigenvalue offers the interpreter an enhanced version of the vertical gravity gradient which is demonstrated with model data and applied to FALCON airborne gravity gradiometer data from the Perth Basin, Australia

**Key words:** Gravity, gradient, tensor, eigenvalues.

## INTRODUCTION

The gravity gradient tensor can be represented by a  $3 \times 3$  real traceless symmetric matrix in source free regions. The method for obtaining the eigenvalues of a general  $3 \times 3$  general matrix involves finding the roots of a third order polynomial and has been known for a long time. Pedersen and Rasmussen (1990) exhibit the solutions for our case. Interpreting the eigenvalues has proven to be an extremely difficult task. By identifying the gravity gradient tensor with the tidal tensor (Cevallos, 2016), one can consider the following scenario: In the absence of external forces, a water droplet in outer space is shaped like a sphere; when subjected to a gravitational field gradient the droplet will be shaped like an ellipsoid. How much the droplet stretches and compresses along each axis of the ellipsoid is given by the eigenvalues, the orientation of the axes is given by the eigenvectors.

The purpose of this paper is to examine the mathematical properties, to find physical meaning of the eigenvalues of the gravity gradient tensor and to show an example of how this knowledge can be used in interpretation. There is very large body of work on eigenvalues and eigenvectors of tensors, in particular tensors represented by real symmetric matrices: Stress, strain, diffusion, conductivity, etc. For example, an instance of this, is the normalized source strength calculated from the eigenvalues of the magnetic gradient tensor (Clark 2012). It is always possible to write a tensor as the sum of a symmetric and an antisymmetric part. A real symmetric tensor can always be transformed to a real diagonal tensor expressed in a particular coordinate system formed by principal directions, principal components or eigendirections as they might be called. There is also a large body of work (a fair amount of it proprietary) on the acquisition and processing of airborne gravity gradient data; these procedures change with different acquisition systems, have different sensitivities, parameters, noise characteristics, interpolation and filtering schemes. Reviewing tensor eigenvalues and eigenvector theory or acquisition and processing techniques is beyond the scope of this paper.

I will present the basic, required definitions of the gravity gradient tensor eigenvalues and invariants as proposed by Pedersen and Rasmussen (1990) and illustrate their main properties when applied to synthetic data and field data.

## THEORY

Define the potential field as a function of position  $\Phi = \Phi(x, y, z)$  in the three orthogonal directions  $x, y,$  and  $z$ ; the gravity field is then represented by a three component vector  $\Phi_k$ : ( $k = x, y, z$ ) and the gravity gradient tensor  $\Psi$  by a matrix  $\Phi_{ij}$ : ( $i, j = x, y, z$ ) where the subscripts indicate partial differentiation with respect to the subscripted variable.

$$\Psi = \begin{pmatrix} \Phi_{xx} & \Phi_{xy} & \Phi_{xz} \\ \Phi_{yx} & \Phi_{yy} & \Phi_{yz} \\ \Phi_{zx} & \Phi_{zy} & \Phi_{zz} \end{pmatrix} \quad (1)$$

The gravity gradient tensor is symmetric, that is,  $\Phi_{ij} = \Phi_{ji}$ , and its trace is zero in source-free regions, that is,  $\Phi_{xx} + \Phi_{yy} + \Phi_{zz} = 0$ . The characteristic equation for determining the eigenvalues  $\lambda_i$  ( $i = 1, 2, 3$ ) is

$$\lambda^3 + I_1 \lambda - I_2 = 0, \quad (2)$$

where

$$I_1 = \Phi_{xx} \Phi_{yy} + \Phi_{yy} \Phi_{zz} + \Phi_{xx} \Phi_{zz} - \Phi_{xy}^2 - \Phi_{yz}^2 - \Phi_{xz}^2, \quad (3)$$

$$I_2 = \Phi_{xx} (\Phi_{yy}\Phi_{zz} - \Phi_{yz}^2) + \Phi_{xy} (\Phi_{yz}\Phi_{xz} - \Phi_{xy}\Phi_{zz}) + \Phi_{xz} (\Phi_{xy}\Phi_{yz} - \Phi_{xz}\Phi_{yy}), \quad (4)$$

where  $I_2$  is  $\det(\Psi)$ , are invariants under any coordinate transformation and  $I_1 \leq 0$ .  
Let  $Q = -I_1/3$  and  $R = I_2/2$ , then Equation 2 has the real roots (Nickalls, 1993; Kindlmann, 2004)

$$\lambda_1 = 2\sqrt{Q} \cos\Theta, \quad (5)$$

$$\lambda_2 = 2\sqrt{Q} \cos(\Theta - 2\pi/3), \quad (6)$$

$$\lambda_3 = 2\sqrt{Q} \cos(\Theta + 2\pi/3), \quad (7)$$

where

$$\Theta = (1/3) \arccos(R/\sqrt{(Q^3)}), \quad (8)$$

and

$$\lambda_1 \geq \lambda_2 \geq \lambda_3. \quad (9)$$

From Equation 8 it can be observed that the range of  $\Theta$  is bounded, as  $R/\sqrt{(Q^3)}$  varies in the interval  $[-1, 1]$   $\Theta$  varies in the interval  $[\pi/3, 0]$  (Kindlmann, 2004).

The eigenvalues can be displayed using the so called eigenvalue wheel used by Nickalls (1993) and Kindlmann (2004) (Figure 1). The wheel allows visualization of the magnitude ( $2\sqrt{Q}$ ) and the phase angles of the three eigenvalues. The terms magnitude and phase in the context of the gravity gradient tensor or tidal tensor have been used before by FitzGerald et al. (2007) and FitzGerald et al. (2009), however the meaning of the terms in their work is different as they refer to eigenvalues and eigenvectors linked via a quaternion representation. Here, I am referring exclusively to the eigenvalues.

In practice, the eigenvalues and, to a lesser degree, the invariants have proven to be difficult to interpret, largely due to the fact that no physical meaning has been attached to them. There are many ways to parametrize three eigenvalues of zero sum in terms of two invariants, the way shown in Equations 5, 6 and 7 enables us to assign physical meaning to the eigenvalues through the understanding of  $2\sqrt{Q}$  and  $\Theta$ .

In general relativity, one of the most basic curvature invariants is the Kretschmann scalar (Stephani et al., 2009). The Kretschmann scalar is defined as the sum of squares of all the components of a given tensor. The Riemann curvature tensor (Misner et al., 1973; Schutz, 1985) is a four-index tensor that is extensively used in general relativity. For the special case when the Riemann curvature tensor reduces to the Newtonian tidal tensor (i.e. the gravity gradient tensor), the Kretschmann scalar is

$$K = -2I_1 = 6Q. \quad (10)$$

As the Kretschmann scalar is proportional to the amount of curvature, it is used in gravitational theory to calculate where the gravitational field is singular (Gkigkitzis et al., 2014; Abdelqader, 2013). In our case, it is the 3-D equivalent of Casorati's curvature (Marussi, 1979) that is used to calculate the curvature of surfaces such that when the surface is a flat plane it is equal to zero. Mathematically, the Kretschmann scalar is equal to the square of the Frobenius norm (Golub and van Loan, 1996).

Pedersen and Rasmussen (1990) define the dimensionless quantity  $I$  as

$$0 \leq I = -[(I_2/2)^2] / [(I_1/3)^3] \leq 1. \quad (11)$$

They point out, that when  $I$  is equal to zero it is an indicator of two dimensionality of the source, although it is not a sufficient condition as there are three dimensional cases where it is also equal to zero. They also show that for a point source  $I$  is equal to one. Substitution of  $Q$  and  $R$  in Equation 11 yields

$$I = (R/\sqrt{(Q^3)})^2. \quad (12)$$

Equations 5 to 12 give intuitive meaning to the eigenvalues of  $\Psi$ . For example, we can now think of the eigenvalues as projections derived from the same magnitude (or length) with different phases. It also means that we do not need to look at the three eigenvalues ( $\lambda_i$ ) (of which only two are independent), but rather at the quantities  $2\sqrt{Q}$  and  $\Theta$ . Examination of the magnitude  $2\sqrt{Q}$  and the phase  $\Theta$  and their spatial behaviors should yield source position curvature information (horizontal location, edges, etc.) in one case and indications or clues of source nature (type of contrast, shapes, etc.) in the other.

It is interesting to note that expanding invariant  $I_2$  such that

$$I_2 = \det(\Psi) = \lambda_1\lambda_2\lambda_3 = (2\sqrt{Q})^3(\cos\Theta)[\cos(\Theta - 2\pi/3)][\cos(\Theta + 2\pi/3)], \quad (13)$$

and using the trigonometric identity

$$\cos 3\Theta = 4\cos^3\Theta - 3\cos\Theta, \quad (14)$$

yields

$$I_2 = [(2\sqrt{Q})^3/4]\cos(3\Theta). \quad (15)$$

Mathematically, Equations 13 and 15 show that except for the  $1/4$  factor in Equation 15 the multiplication of the eigenvalues that yields  $I_2$  is similar to a complex number multiplication (product of magnitudes and addition of phases) (Figure 1).

## MODELING

Basic visualization of the horizontal variations of  $2\sqrt{Q}$  and  $\Theta$  can be achieved using the synthetic model used in Cevallos et al. (2013). In the model, two  $1 \text{ km}^3$  model cubes were assigned density contrasts of + (left body) and - (right body)  $1.0 \times 10^3 \text{ kg/m}^3$  respectively in a  $2.67 \times 10^3 \text{ kg/m}^3$  background density. The cubes are separated by 1 km and have a depth to top of 100 m.

The eigenvalues and  $\Phi_{zz}$  for comparison are shown in Figures 2, 3, 4 and 5. They show the typical behavior of what is known as the positive asymmetric eigenvalue  $\lambda_1$ , the symmetric eigenvalue  $\lambda_2$  and the negative asymmetric eigenvalue  $\lambda_3$  (Dransfield; 1994) and  $\Phi_{zz}$ . The magnitude  $2\sqrt{Q}$  (Figure 6) shows the expected symmetric behavior, good positioning of the sources and a good definition of the boundaries. The phase  $\Theta$  (Figure 7) shows the expected anti symmetric behavior and a complex point source behavior away from

the bodies and in arcs that go from corner to corner avoiding the edges of the bodies. It can now be seen why the eigenvalues are so difficult to interpret: The phase  $\Theta$  shows a very complex spatial behavior even for a simple case like the one modeled here. This fact discourages the use of  $\Theta$  in interpretation. What would be desirable is that instead of having the magnitude  $2\sqrt{Q}$  multiplied by  $\cos\Theta$ ,  $\cos(\Theta - 2\pi/3)$ , and  $\cos(\Theta + 2\pi/3)$  to generate the eigenvalues, another quantity could be used such that interpretation becomes easier. A natural candidate is the shape index (SI) (Koenderink and van Doorn, 1992; Roberts, 2001; Cevallos et al., 2013; Cevallos, 2014):

$$SI = (2/\pi)\arctan\{\Phi_{zz}/[(\Phi_{xx} - \Phi_{yy})^2 + 4\Phi_{xy}^2]^{1/2}\}. \quad (16)$$

The shape index is a smooth continuous function that like the cosine function has values defined in the range  $[-1, 1]$ . It is related to the type of source as it describes the shape of the equipotential surfaces that the sources generate. A modified phase eigenvalue can then be defined as:

$$\lambda_{si} = 2\sqrt{Q} SI. \quad (17)$$

The shape index and the modified phase eigenvalue  $\lambda_{si}$  of the synthetic cubes are shown in Figures 8 and 9. The preservation of the sign of the density contrast is clearly illustrated in Figure 9 compared with the magnitude of  $2\sqrt{Q}$  illustrated in Figure 6.

I have found the modified phase eigenvalue useful in interpretation as it gives a slightly sharper definition of the edges of the sources than the eigenvalues or the vertical gravity gradient  $\Phi_{zz}$ .

As the gravity gradient tensor  $\Psi$  is symmetric and is traceless, it has five independent quantities to interpret. Interpreting two quantities: the invariants, the eigenvalues, the modulus and the phase, or the modulus and the shape index cannot give a complete description of sources. There are three more quantities to consider, the ones associated with the three eigenvectors, namely three angles.

### APPLICATION

The modified phase eigenvalue was calculated for the FALCON® AGG data from the central part of the Perth Basin, Western Australia (Kovac et al., 2016) (Figure 17).

The Perth Basin is part of the continental margin of south-western Australia. It is bordered by the Archean Yilgarn Craton to the east, the Southern Carnarvon Basin to the north, the Bight Basin to the southeast and oceanic crust of the Indian and Southern Oceans to the west and south, respectively. The creation of the basin is related to the breakup of Gondwanaland and the formation of the Indian Ocean. The basin contains up to 15 km of mid-Carboniferous to Lower Cretaceous sedimentary rocks (Thomas, 2014), which trace a long-lived, mostly non-marine depositional environment with occasional marine incursions (FrOG Tech, 2006; Playford et al., 1976). The structural architecture of the Perth Basin is the result of oblique rifting during the Permian, Late Triassic to Early Jurassic and Middle Jurassic to Early Cretaceous, superimposed over pre-existing basement terrains. Metamorphic rocks of the Mesoproterozoic to Neoproterozoic Pinjarra Orogeny, which are exposed in the Leeuwin, Mullingarra, and Notthampton Inliers, determine the geological basement of the Perth Basin. The survey was flown east-west with a nominal flying height of 100 m with 1000 m line spacing, using a flight line to tie line ratio of 10:1. For interpretation purposes, gravity data was terrain corrected using density values of  $1.4 \times 10^3 \text{ kg/m}^3$  in the western part, and  $2.0 \times 10^3 \text{ kg/m}^3$  in the eastern part (Figure 17). As the eastern part contains the most promising identified leads and gas discoveries all the following images were calculated using  $2.0 \times 10^3 \text{ kg/m}^3$  terrain corrected data. The survey identified large structural leads as the target of future gas exploration including infill 2D seismic acquisition and that the prospectivity of some of the leads increased significantly with gas discovery wells (Kovac et al., 2016).

Figures 18, 19, 20 and 21 (all figures have illuminated shading from the northeast with an elevation of 45 degrees) show the vertical gravity gradient  $\Phi_{zz}$ , magnitude  $2\sqrt{Q}$ , shape index SI and modified phase eigenvalue  $\lambda_{si}$ . Comparison between the  $\Phi_{zz}$  (Figure 18) and the  $\lambda_{si}$  (Figure 21) images shows two general results and an observation:

- Comparable dynamic ranges.
- $\lambda_{si}$  is sharper than  $\Phi_{zz}$ , that is,  $\lambda_{si}$  appears to be a subtle enhanced version of  $\Phi_{zz}$ .
- There appear to be artifacts associated with line direction (east west) in the central eastern part of the survey.

To more clearly illustrate the differences between the  $\Phi_{zz}$  and  $\lambda_{si}$  I have zoomed into the central part of the survey for the images in Figures 18 and 21 and put them side by side in Figure 22 (some pixelation can be observed).

As  $\Phi_{zz}$  forms the basis of all gravity gradient interpretations, the second result is significant. It is important to note that the result is not obtained by taking spatial derivatives of gradients, for example, taking the first vertical derivative of  $\Phi_{zz}$  or  $2\sqrt{Q}$ , a procedure that looks good when applied to with model data, but when applied to real cases it is not satisfactory due to the concurrent enhancement of noise.

The geological significance of the last result is the enhancement of particular trends, for example: north south in the center of the area, northwest southeast in the west of the area and east-west in the center of the area. If these enhanced trends had been available at the time of the interpretation it is unlikely they would have changed the interpretation results, but they would have made them easier to obtain and changed their relative importance.

Why is  $\lambda_{si}$  sharper than  $\Phi_{zz}$ ? As all the eigenvalues have the common magnitude term  $2\sqrt{Q}$ , if a diagonal matrix representing the tensor in an eigenvector coordinate system is rotated to a (x, y, z) coordinate system, all the tensor components  $\Phi_{ij}$  (including  $\Phi_{zz}$ ) will be linear combinations of the eigenvalues. They will all therefore have the common term  $2\sqrt{Q}$  multiplied by coefficients comprising products and sums of sines and cosines of the three rotation angles (yaw, pitch and roll) and the phase  $\Theta$ . For the  $\Phi_{ij}$  in general, this process will alter and most likely diminish the original resolution of  $2\sqrt{Q}$ .

It is encouraging that a simple scheme of phase substitution yields such model and application results. It is clear there are at least two more schemes to propose and test: other angles as phases and noise mitigated horizontal gradients of the magnitude.

## CONCLUSIONS

The concept of tidal tensor gives meaning to the eigenvalues and eigenvectors of the gravity gradient tensor. The eigenvalues can be expressed as functions of a magnitude and a phase. This decomposition gives particular physical meaning to the eigenvalues: the magnitude measures the amount of curvature and the phase is related to the type of source. The modified phase eigenvalue proposed here, offers the interpreter an enhanced version of the vertical gravity gradient.

## REFERENCES

- Abdelqader, M., 2013, Analysis and Visualization of Exact Solutions to Einstein's Field Equations: PhD Thesis, Queen's University Kingston, Ontario, Canada.
- Cevallos, C., 2016, Interpreting the direction of the gravity gradient tensor eigenvectors: Their relation to curvature parameters of the gravity field: *Geophysics*, **81**, 3, G49–G57.
- Cevallos, C., 2014, Automatic generation of 3D geophysical models using curvatures derived from airborne gravity gradient data: *Geophysics*, **79**, 5, G49–G58.
- Cevallos, C., P. Kovac, and S. J. Lowe, 2013, Application of curvatures to airborne gravity gradiometry data in oil exploration: *Geophysics*, **78**, 4, G81–G88.
- Clark, D. A., 2012, New methods for interpretation of magnetic vector and gradient tensor data I: eigenvector analysis and the normalized source strength: *Exploration Geophysics*, **43**, 267–282.
- Dransfield, M. H., 1994, Airborne Gravity Gradiometry: PhD Thesis, The University of Western Australia.
- FitzGerald, D.J., D. Argast, and H. Holstein, 2009, Further developments with full tensor gradiometry datasets: ASEG Extended Abstracts 2009, 20th Geophysical Conference, 1–7.
- FitzGerald, D.J., H. Holstein, and D. Argast, 2007, The amplitude / phase treatment of full tensor gradiometry: ASEG Extended Abstracts 2007, 19th Geophysical Conference, 1–4.
- FrOG Tech, 2006, OZ SEEBASE Proterozoic basins study, Report to Geoscience Australia by FrOG Tech Pty, Ltd.: accessed February 8, 2013, <http://www.frogetech.com.au/products/oz-seebase>.
- Gkigkitzis, I., I. Haranas, and O. Ragos, 2014, Kretschmann invariant and relations between spacetime singularities entropy and information: *Physics International* **5**(1), 103–111.
- Golub, G. H., and C. F. Van Loan, 1996, Matrix Computations, 3rd Edition: The Johns Hopkins University Press, 55.
- Kindlmann, G., 2004, Visualization and Analysis of Diffusion Tensor Fields: PhD Thesis, University of Utah.
- Koenderink, J. J., and A. J. van Doorn, 1992, Surface shape and curvature scales: *Image and Vision Computing*, **10**, 557–564.
- Kovac, P., C. Cevallos, and J. Feijth, 2016, Targeting oil and gas in the Perth Basin using an airborne gravity gradiometer: *First Break*, **34**, 51–58.
- Li, X., 2015, Curvature of a geometric surface and curvature of gravity and magnetic anomalies: *Geophysics*, **80**, 1, G15–G26.
- Marussi, A., 1979, The tidal field of a planet and the related intrinsic reference systems: *Geophys. J. R. astr. Soc.*, **56**, 409–417.
- Misner, C. W., K. S. Thorne, and J. A. Wheeler, 1973, Geodesic Deviation and the Riemann Curvature Tensor: *Gravitation*, San Francisco: W. H. Freeman, 218–224.
- Nickalls, R. W. D., 1993, A new approach to solving the cubic: Cardan's solution revealed: *The Mathematical Gazette*, **77**, 354–359.
- Pedersen, L. B., and T. M. Rasmussen, 1990, The gradient tensor of potential field anomalies: Some implications on data collection and data processing of maps: *Geophysics*, **55**, 1558–1566.
- Playford, P. E., A. E., Cockbain, and G. H., Low, 1976, The Geology of the Perth Basin, Bulletin 124, Western Australia Geological Survey.
- Roberts, A., 2001, Curvature attributes and their application to 3D interpreted horizons: *First Break*, **19**, 85–100.
- Schutz, B. F., 1985, Riemann Tensor and Geometric Interpretation of the Riemann Tensor: A First Course in General Relativity, Cambridge, England: Cambridge University Press, 210–214.
- Stephani, H., D. Kramer, M. Maccallum, C. Hoenselaers, and E. Herlt, 2009, Exact Solutions of Einstein's Field Equations, 2nd ed.: Cambridge Monographs on Mathematical Physics, Cambridge University Press, 112–128.
- Thomas, C. M., 2014, The Tectonic Framework of the Perth Basin: Current Understanding, Record 2014/14, Department of Mines and Petroleum.

## FIGURES

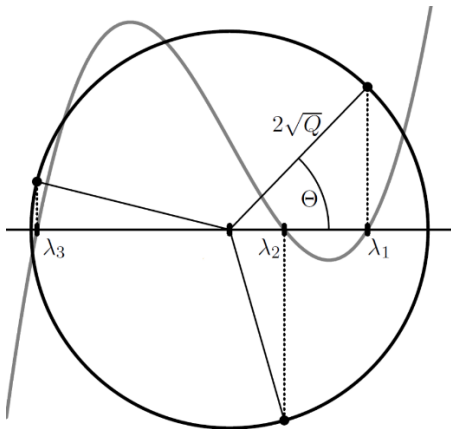


Figure 1. Diagram of cubic characteristic polynomial (in gray), its roots, and the invariants required for determining the roots with Equations 5, 6 and 7 (after Kindlmann, 2004).

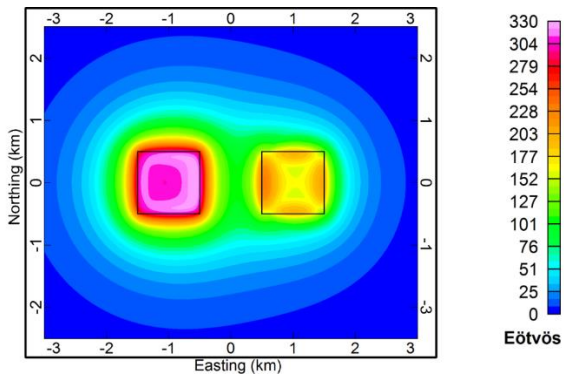


Figure 2. Eigenvalue  $\lambda_1$ , over synthetic model cubes, shown by black outlines (denser body on the left).

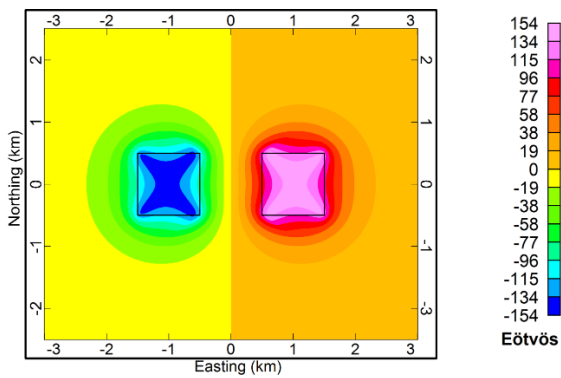


Figure 3. Eigenvalue  $\lambda_2$ , over synthetic model cubes, shown by black outlines (denser body on the left).

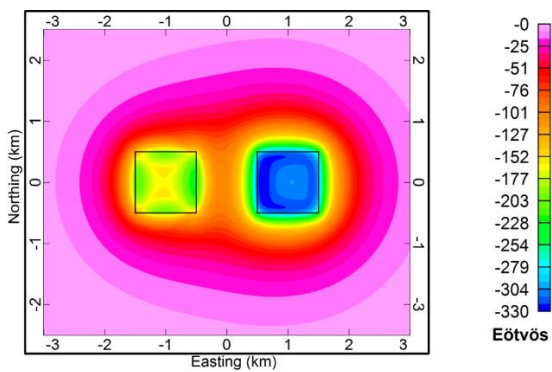


Figure 4. Eigenvalue  $\lambda_3$ , over synthetic model cubes, shown by black outlines (denser body on the left).

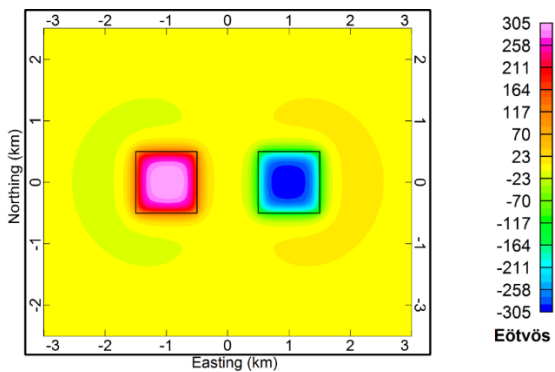


Figure 5. Vertical gravity gradient  $\Phi_{zz}$ , over synthetic model cubes, shown by black outlines (denser body on the left).

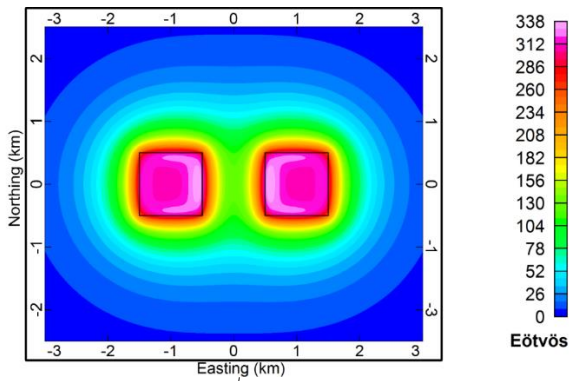


Figure 6. Magnitude  $2\sqrt{Q}$ , over synthetic model cubes, shown by black outlines (denser body on the left).

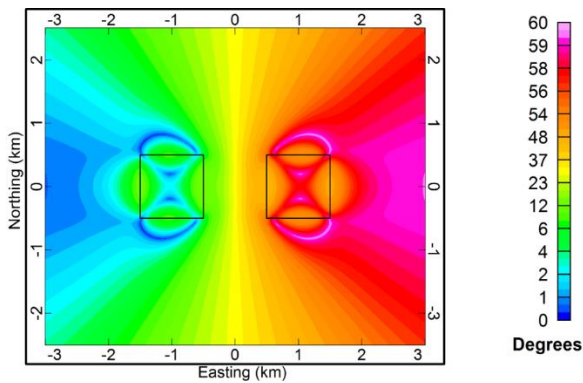


Figure 7. Phase  $\Theta$ , over synthetic model cubes, shown by black outlines (denser body on the left).

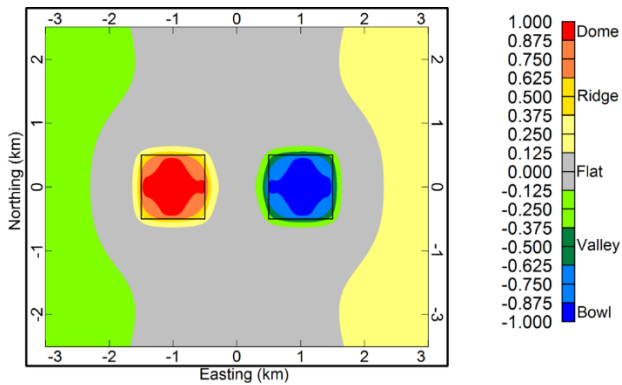


Figure 8. Shape index SI, over synthetic model cubes, shown by black outlines (after Cevallos et al., 2013) (denser body on the left).

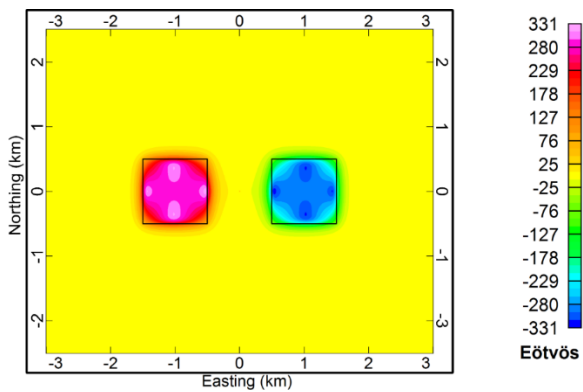
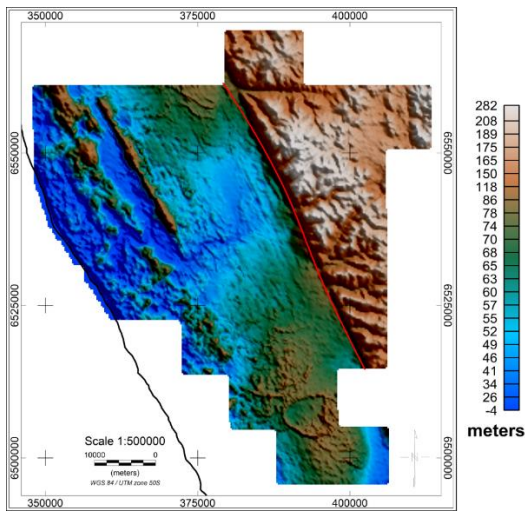
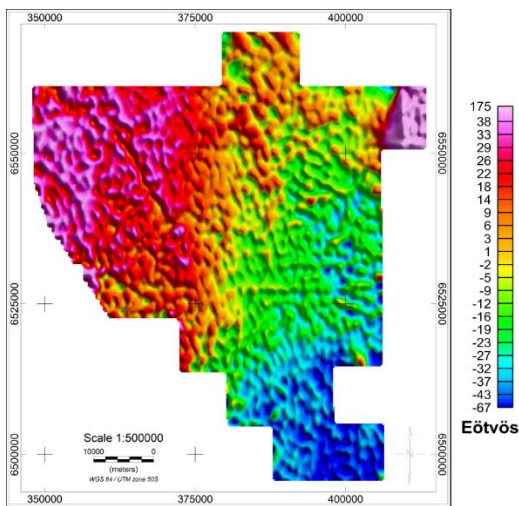


Figure 9. Modified phase eigenvalue  $\lambda_{si}$ , over synthetic model cubes, shown by black outlines (denser body on the left).



**Figure 17.** Location of the Perth survey area over topography. Coastline in black outline. Terrain corrections used a density value of  $1.4 \times 10^3 \text{ kg/m}^3$  to the west of the red outline and a density value of  $2.0 \times 10^3 \text{ kg/m}^3$  to the east of the red outline. Sunshaded from the NE with a sun elevation of  $45^\circ$ .



**Figure 18.** Vertical gravity gradient  $\Phi_{zz}$ , of survey area. Sunshaded from the NE with a sun elevation of  $45^\circ$ .

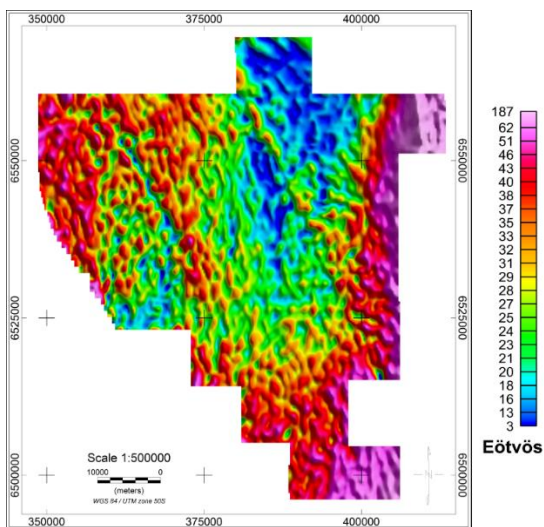


**Figure 19.** Magnitude  $2\sqrt{Q}$ , over survey area. Sunshaded from the NE with a sun elevation of  $45^\circ$ .

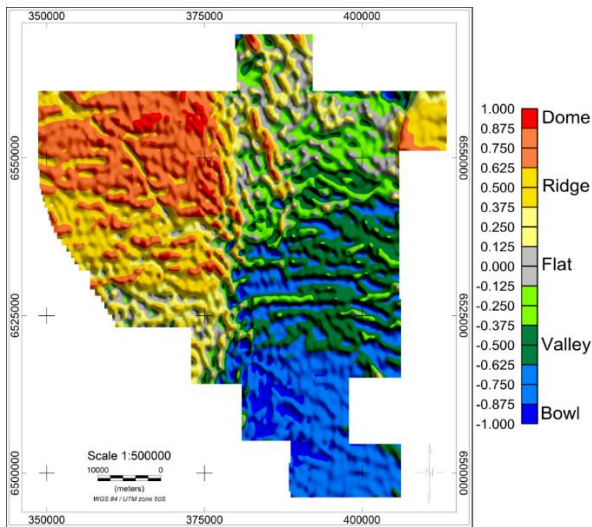


Figure 20. Shape Index SI of equipotential surfaces, over survey area. Sunshaded from the NE with a sun elevation of 45°.

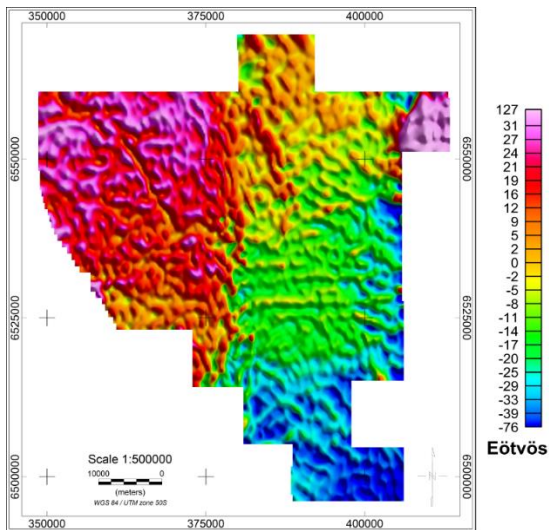


Figure 21. Modified phase eigenvalue  $\lambda_{si}$ , over survey area. Sunshaded from the NE with a sun elevation of 45°.

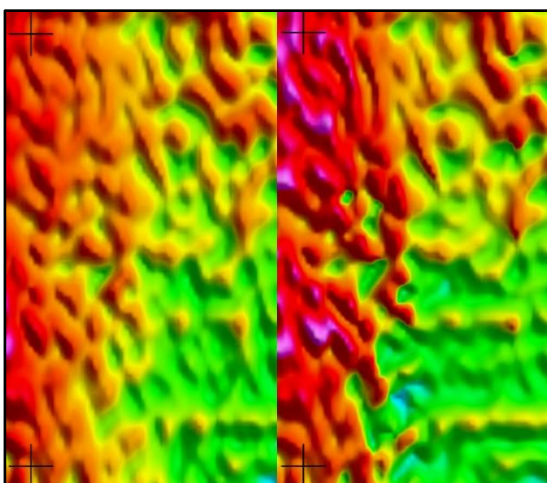


Figure 22. Vertical gravity gradient  $\Phi_{zz}$  (left) and modified phase eigenvalue  $\lambda_{si}$  (right), over central survey area. Sunshaded from the NE with a sun elevation of 45°.